Boundary-Layer Meteorology (2025) 191:11
https://doi.org/10.1007/s10546-025-00899-9

RESEARCH ARTICLE

Wind Extremes over Built Terrain: Characterization and Geometric Determinants

Jing Wang[1] · **Maider Llaguno-Munitxa**[2] · **Qi Li**[3] · **Marco Giometto**[4] · **Elie Bou- Zeid**[1]

Received: 12 July 2024 / Accepted: 6 January 2025

Abstract

Cities feature complex and heterogeneous topographies that create highly-variable airflow patterns and dynamics. The resulting extreme high and low winds challenge urban design's quest for maintaining a safe and comfortable environment. This study investigates these urban wind extrema by conducting large-eddy simulations (LESs) in four American neighborhoods with distinct topographic features and links the resulting winds to geometric indicators. By analyzing the profile and spatial variation of the wind extrema, the simulations illustrate that gust zones tend to occur along wind-oriented streets and on both sides of high-rise buildings, while stagnation zones are mostly located in the lee of tall or wide buildings. Potential geometric parameters explaining these winds extrema are investigated, including the plan and frontal area fraction and the sky view factor. These findings advance our ability to predict wind conditions solely based on urban geometry, and ultimately to design more resilient, sustainable, and livable cities.

Keywords Air exchange · Dispersive flux · Sky view factor · Stagnation zones · Wind gusts

1 Introduction

As of 2021, about 56% of the world's total population is living in urban agglomerations, and this fraction is expected to reach 68% by 2050 (UN-DESA 2018). As cities expand to house this growing population (Angel 2012), they are bearing the brunt of climate change since their form (geometric and topographic complexity), fabric (the unique properties of materials used in buildings and infrastructure), and function (the human activities that drive energy demand and anthropogenic heat releases) can significantly exacerbate heat and rainfall extremes,

✉ Elie Bou- Zeid
ebouzeid@princeton.edu

1 Department of Civil and Environmental Engineering, Princeton University, Princeton, NJ 08544, USA

2 Faculty of Architecture, Architectural Engineering and Urban Planning, UCLouvain, Place du Levant 1, 1348 Ottignies-Louvain-la-Neuve, Belgium

3 School of Civil and Environmental Engineering, Cornell University, Ithaca, NY 14853, USA

4 Department of Civil Engineering and Engineering Mechanics, Columbia University, New York, NY 10027, USA

Published online: 07 February 2025

among other geophysical hazards (Li and Bou-Zeid 2013; Ryu et al. 2016; Dodman et al. 2022; Glavovic et al. 2022). Therefore, as the fate of the human race is now closely related to the urban environment where risks are ever increasing, better design and planning of cities is more essential than ever.

An important object of such urban design is airflow, which is a critical factor for street ventilation, pedestrian's comfort and health, and wind impacts on infrastructure (Du and Mak 2018; Lee and Ham 2021). On the one hand, the gusts (extreme high winds) can produce disquieting noise, threaten the performance of drones, impede pedestrian's ability to maintain a body balance, or even damage infrastructures and then produce lethal flying debris (Hunt et al. 1976; Blocken and Carmeliet 2004; Blocken et al. 2016; Nesta 2018; Mairaj et al. 2019). An adult pedestrian can feel uncomfortable while walking when the wind speed exceeds 5 m/s and it becomes dangerous when it surpasses about 15 m/s (He and Song 1999; Blocken et al. 2016; Oke et al. 2017). On the other hand, the extreme, very low wind speed reduce air exchange between the flow in and above the canopy, thus leading to poor ventilation and trapping the pollution and heat near the ground (Britter and Hanna 2003; Li et al. 2006; Baklanov et al. 2009; Salizzoni et al. 2011; Panagiotou et al. 2013; Llaguno-Munitxa and Bou-Zeid 2018).

The wind engineering literature has traditionally focused on highly idealized geometrical representation of buildings consisting of identical 3D cubes or 2D cubical ribs (Brown et al. 2001; Kanda et al. 2004; Coceal et al. 2007; Anderson et al. 2015; Li et al. 2020a; Nazarian et al. 2020). Subsequently, cubes with varied heights and footprints were considered, but the the studies were often based on simulations over simplified building canopies and continued to center around the aggregate surface drag coefficient and the reduction in wind speed (Shaikh Salim et al. 2011; Zhu et al. 2017; Zhu and Anderson 2018; Kawaminami et al. 2018; Sützl et al. 2021). There is, however, an accelerating realization of the need to shift to physical or numerical experiments over real or realistic urban canopies to better understand the spatial variability of the flow, turbulence, and ventilation in actual cities, and the corresponding literature is growing (Xie and Castro 2009; Bou-Zeid et al. 2009; Ahmad et al. 2017; Kurppa et al. 2018; Akinlabi et al. 2022; Lu et al. 2023b).

Previous studies indicated that building height variability (Millward-Hopkins et al. 2012; Kawaminami et al. 2018), building density (Kanda et al. 2013), arrangement complexity, and street orientation and aspect ratio can be important factors for the temporally-averaged (mean) wind velocities and gas concentrations (Arkon and Özkol 2014; Takemi et al. 2020). The frontal area fraction (λ_f) and plan area fraction (λ_p) have been identified as key parameters that can encode some of these geometric properties and influence air flow, as well as thermal comfort and air quality in cities (Li et al. 2020b). Previous literature has shown that the mean wind speed decreases with the gross building coverage ratio, which corresponds to λ_p (Kubota et al. 2008). The turbulent gust ratio also decreases with λ_p for realistic urban areas (Ahmad et al. 2017). Ng et al. (2011) demonstrated a strong correlation between the ground coverage ratio (GCR) and λ_f, and established that GCR can be used to predict the pedestrian level ventilation. Other researchers have attempted to derive new parameters combining λ_p with other metrics to provide a predictive framework for wind speed (Yuan and Ng 2012). Furthermore, some studies have proposed completely new geometric parameters to characterize winds, such as alignedness and variability of building facet orientation (Lu et al. 2023a), to better represent the connectivity and predict canopy-averaged flow properties. For example, to help model the sectional drag coefficient more effectively, Simón-Moral et al. (2014) proposed two novel geometry parameters, the sheltering parameter λ_s and the channeling parameter λ_{ch}.

Despite this expanding research, a full understanding and adequate predictive skill for wind extremes in urban canopies remain elusive. Unlike vegetation canopies, urban canopies are more heterogeneous and the buildings, especially the taller ones, can induce both ‘local’ and ‘non-local’ effects (Goulart et al. 2018; Lim et al. 2022). These tall buildings often protrude into the canonical outer layer of the ABL, and their variability produces turbulent mixing that sustains vertical fluxes of mass, momentum, and heat by the chaotic eddies. Another vertical mixing and transport mechanism arising from the presence of canopy heterogeneity is the spatial covariance of the time-averaged flow fields (for example, of vertical velocity and temperature) that produces the so-called dispersive fluxes (Martilli et al. 2013; Li and Bou-Zeid 2019). These important transport mechanisms are strongly influenced by the geometry and inhomogeneity of the urban canopy (Giometto et al. 2016; Akinlabi et al. 2022). Also altered by these canopy characteristics are the mean profiles of wind and scalars (temperature, humidity, or pollutant concentrations), which are quite distinct from their idealized cuboid canopy counterparts. The wind profiles in idealized cuboid setups are often modeled as an exponential or linear function within the canopy, blending into the logarithmic law above (Macdonald 2000; Roth 2000; Coceal and Belcher 2004; Chen et al. 2011), and whether such models also apply broadly to realistic building configurations in cities also remains an open questions.

The complex and highly heterogeneous surfaces bring challenges to on-site measurements, making it impossible to collect enough data to capture all spatial features of the flow (Pardyjak and Stoll 2017). Wind tunnel or water flume experiments then become an alternative method for measuring flows in realistic urban canopies (Hertwig et al. 2019; Lim et al. 2022). In the last few decades, however, turbulence-resolving computational fluid dynamics (CFD) simulations have become a powerful tool for studying urban canopy flows. Specifically, despite challenges for the technique that we discuss in the methods section, large eddy simulation (LES) has emerged as the tool of choice for flow simulations in complex domains, as outlined in the vision report for fluid dynamics simulations by NASA (Slotnick et al. 2014). Urban LES applications have thus expanded rapidly, as reviewed recently by Stoll et al. (2020).

Therefore, LES will be used to address some of the aforementioned gaps in our understanding of flow over real cities and to better predict extremes and how they are dictated by urban geometry. Specifically, this study sets out to answer the following questions:

- What fluid dynamical indicators are well suited for characterizing gust and stagnation zones in cities?
- How do mean and extreme wind statistics vary between cities with distinct urban characteristics?
- What urban geometrical attributes can help predict gust and stagnation zones within a given city?

Full building layouts are required to investigate these questions using LES. High resolution digital surface maps (DSMs) are now a common tool to represent the topographies in urban areas (Zhou 2017) and are used in this paper. In the next section, we briefly introduce these DSM data and the LES approach. We also validate the performance of our code for various roof shapes and real cities. In Sect. 3, we present LES results and characterize the spatial and temporal wind variability for a single city. In Sect. 4, we analyze three parameters which quantify important geometry features, with a focus on the relationship between building geometries and the extremes. In the last section, we synthesize the key results and present the conclusions.

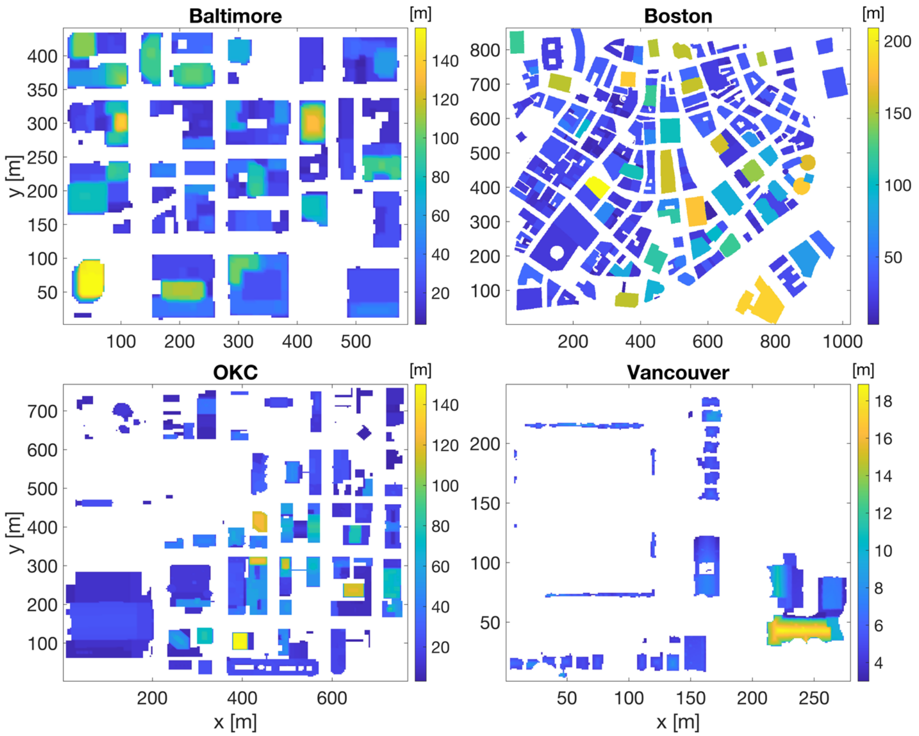

Fig. 1 Pseudocolor plot of surface elevation above ground level, showing building geometries. The corresponding satellite images are shown in Online Resource 1

2 Data and Methods

2.1 DSM Data

The digital surface maps (DSMs) for 4 real cities (Baltimore (Day et al. 2013), Boston (OpenStreetMap contributors 2017), Oklahoma City (OKC) (García-Sánchez et al. 2014) and Vancouver (Giometto et al. 2017)) were used for the present simulations. We selected sections in these cities to yield distinct geometric features, as illustrated in Fig. 1 (the satellite images corresponding to the DSMs are shown in Online Resource 1). More details on the DSMs and the statistics of the building height h can be found in Table 1. The average building height is computed as $h_{mean} = \Sigma_{i,j} d_{i,j}/(N_x \times N_y)$; where $d_{i,j}$ is the matrix of surface elevations from the DSM, and N_x and N_y are the grid numbers in the streamwise and spanwise directions. For convenience the areas are henceforth referred as S_{Bal}, S_{Bos}, S_{OKC}, S_{Van}. In S_{Bal} and S_{Bos}, buildings are densely distributed, but S_{Bos} buildings are generally taller and have an irregular layout. Buildings in S_{OKC} are mainly mid-rise and spaced out. S_{Van} features 2-storey houses, with large unbuilt areas. For all these cities we assume the terrain is flat.

All low-rise obstacles with height $< 3m$ were removed because they cannot be resolved adequately by the numerical grid. These low-rise obstacles are assumed to consist mainly of objects other than buildings (cars, trees, small structures, etc.). In addition, the building façades shown in Fig. 1 are already smoothed to remove very small features or noise in the

Table 1 Relevant statistics of buildings

	h_{mean} (m)	h_{max} (m)	h_{min} (m)	σ_h (m)	μ_3	Resolution (m)
Boston	57.0	209.0	3.0	51.4	1.5	1
Baltimore	41.6	156.4	3.0	33.9	1.3	1
OKC	26.4	150.0	3.0	25.1	2.2	1
Vancouver	6.7	18.9	3.0	3.6	1.8	0.5

h_{mean} is the avearge building height; h_{max} and h_{min} are the tallest and shortest building height in each domain; σ_h is the standard deviation; and μ_3 is the skewness of building heights. The resolution listed here is for the DSM data not the LES grid

data and ensure the simulations are not contaminated by poorly resolved geometry (this was especially needed for the Baltimore dataset). Our findings and conclusions, however, are minimally dependent on the fidelity of the DSMs. Instead of simulating the exact velocity at a specific real-world location, we are aiming to educe the relationship between extreme winds and geometric features. Therefore, any realistic DSM is suitable even if it is not an exact replica of the city.

2.2 LES Model and Building Representation

The DSMs are first converted into inputs for the LES (which requires a signed distance function evaluated at each grid point), where the buildings are resolved as bluff bodies using an immersed boundary method (IBM) (Chester et al. 2007; Bou-Zeid et al. 2009; Li et al. 2016a; Giometto et al. 2017). IBM is now widely used for urban fluid mechanics due to its relatively low computational cost and its ability to use Cartesian meshes that are simpler to implement than body conforming ones (Mittal and Iaccarino 2005; Chester et al. 2007). IBM computes the force B_i required to have zero velocity inside the solid, and this in turn generates the pressure force in the fluid domain that the structure would be imposing on the flow. All simulations here use a uniform Cartesian mesh. The spatially filtered mass and momentum budget equations for incompressible Newtonian flows as solved in the code are:

$$\frac{\partial \hat{u}_i}{\partial x_i} = 0, \tag{1}$$

$$\frac{\partial \hat{u}_i}{\partial t} + \hat{u}_j \left(\frac{\partial \hat{u}_i}{\partial x_j} - \frac{\partial \hat{u}_j}{\partial x_i} \right) = -\frac{\partial \hat{p}^*}{\partial x_i} - \frac{\partial \tau_{ij}}{\partial x_j} + \hat{F}_i + \hat{B}_i, \tag{2}$$

where the hat represents filtered quantities; $\hat{u}_i$ is the velocity; x_i is the position vector; $\hat{F}_i$ is the synoptic forcing (i.e. the mean pressure gradient driving the flow); τ_{ij} is the anisotropic part of subgrid-scale (SGS) stress tensor $\sigma_{ij} = \widehat{u_i u_j} - \hat{u}_i \hat{u}_j$; $\hat{p}^*$ is the modified pressure that includes the resolved and SGS turbulent kinetic energy components and is computed as $\hat{p}^* = \hat{p} + (1/2)\hat{u}_j \hat{u}_j + (1/3)\sigma_{kk}$ (σ_{kk} here is the trace of the SGS stress tensor); and $\hat{B}_i$ is the immersed boundary force to represent the buildings. The buoyancy term is ignored since we assume a neutral flow, and thus no energy or scalar budget equation is solved. For notational simplicity, all hats are henceforth omitted since we only deal with filtered quantities. Both equations are normalized by u_*^2/z_i, with z_i equal to the domain height and u_* representing the friction velocity resulting from the total drag (form and friction) of the surface on the flow; this velocity evolves to balance the driving pressure forcing in the LES runs (since the Coriolis force is ignored). The code output is hence also normalized by u_* and z_i, and where it is necessary to dimensionalize the results to give a sense of the magnitudes in real cities, we will use nominal values of $u_* = 1$ m s^{-1}.

The second order Adam-Bashforth scheme is used for time stepping. For spatial differentiation, a second-order centered finite difference method is used on a staggered mesh in the vertical direction, while a pseudospectral method is used for calculating the horizontal derivatives and for test filtering for the SGS model computations. To reduce the Gibbs phenomenon's erroneous oscillations in the solution, the cubic interpolation smoothing developed and tested by Li et al. (2016a) is used. A Lagrangian scale-dependent dynamic subgrid-scale model is used (Bou-Zeid et al. 2005) to close the equations. The detailed steps of the time advancement are shown in Appendix 1.

The top boundary condition is a stress-free impermeable surface in all simulations. The horizontal boundary conditions are numerically and physically periodic in all simulations of real canopies. Since the pseudo-spectral calculations of derivatives and filtering in the horizontal directions require periodic boundary conditions numerically, creating a physically non-periodic domain requires buffer zones and the preparation of an inflow (Li et al. 2016b; Allouche et al. 2023); this is only used in the validation against wind tunnel data in the next subsection. To impose boundary conditions on the fluid at the air-solid interface, a layer of boundary grid points are created at a distance of 1.1Δ (the grid resolution) on the fluid side. Fluid solutions are interpolated onto these points, then an equilibrium wall model is used to compute the stresses on the fluid at these boundary points, and the stress is finally extrapolated/interpolated back to the regular grid (see full detail in Chester et al. (2007)). One major challenge for LES with the buildings resolved is the potential computational cost for matching the high Reynolds numbers (Re) of real urban flows. Despite the continuous advancements in computer hardware and software, resolving the viscous sublayers around the obstacles is still not achievable (Dagnew and Bitsuamlak 2013; Gopalan et al. 2013; Khaled et al. 2021). A wall model is thus required to bypass the inner wall region, where the buffer and viscous sublayer are located. In this study, we use an equilibrium wall model based on the logarithmic law of the wall, as detailed in Li et al. (2016b). This requires specification of the roughness length pertaining to each surface element at the fluid-solid boundary, and in the present study we use $z_0 = 10^{-5}$ m corresponding to smooth facets.

2.3 Evaluation of the LES Model

Our LES code has been widely validated against observations for homogeneous/heterogeneous terrains (Bou-Zeid et al. 2004, 2005), and for stable/unstable boundary layer conditions (Kleissl et al. 2006; Kumar et al. 2006, 2010; Huang and Bou-Zeid 2013). The IBM implementation was also validated against wind tunnel and field studies, but mostly for simple cuboidal geometries (Tseng et al. 2006; Li et al. 2016a, b). With the LES approach adopted here, these previous evaluation studies indicate that the main challenges for achieving high-quality results are the accuracy of the wall model and the ability to resolve the fluid–structure interaction effects on the flow. To resolve this interaction faithfully, ≈ 8 grid points per building dimension are required; this, however, often becomes impractical when simulating large and non-uniform buildings representing real cities. The buildings dimensions are generally ~ 10 m to 100 m, and capturing the flow interaction of the smallest structures with enough grid points is often not feasible. However, these small structures often do not have a significant impact on the mean, and only a limited impact on the simulated turbulence fields (Bou-Zeid et al. 2009). Real buildings also feature round and complex shapes where the flow separation point in the lee of the building is not strongly dictated by the geometry and can

Table 2 Simulation setup parameters for performance evaluations for different roof shapes (note that the actual grid spacing dy is smaller in the high resolution simulation despite the reduced number of grid points since the domain simulated is narrower)

	Building height $H(m)$	# grids per building	$L_x \times L_y \times L_z (m^3)$	$N_x \times N_y \times N_z$
Low res	7.5	10	$360 \times 90 \times 54$	$480 \times 120 \times 72$
High res	7.5	15	$300 \times 54 \times 54$	$600 \times 108 \times 108$

vary with Re; this makes the wall model much more critical for the results (Llaguno-Munitxa and Bou-Zeid 2018). Therefore, in this section we aim to test the performance of the code, with the wall model detailed in Li et al. (2016b), first over non-cuboidal geometries where the location of the flow separation point is not constrained to be over the edges of the buildings, and then for flow over real urban canopies.

First, we will compare the simulated flow patterns for three different roof geometries to results we obtained in previous work (Llaguno-Munitxa et al. 2017) through wind tunnel measurements and simulations using a different LES code (Ansys Fluent). Key simulations parameters are shown in Table 2. We evaluated two different resolutions, 10 grids per building and 15 grids per building. (See Online Resource 2 for a schematic of one simulation domain and geometry with round roofs). We also simulate and evaluate pitched (triangular) and flat roofs with the same maximum building height as for the round geometry shown in the figure. For all simulations, the distance between the inlet (inlet #1 in Llaguno-Munitxa et al. (2017), which applies a laminar and uniform inflow velocity U_{mean} to best mimic the wind tunnel) and the first building is 131.25 m. We should note that since our LES neglects all viscous terms, the exact dimensions of the computational domain are irrelevant (e.g., in comparison to the wind tunnel) since the simulations are assumed to lie in a very high Re-similarity regime, as long as geometric similarity is respected. However, finite Re effects in the measurements can bias the comparison.

Comparisons of the mean (time-averaged) wind ($U_t = \sqrt{\overline{u}^2 + \overline{w}^2}$) and its variance ($\sigma_t^2 = \sigma_u^2 + \sigma_w^2$) in a streamwise-vertical plan (these were identical to the hot wire measurements in the wind tunnel) are conducted along a vertical transect in the middle of the last canyon (in which the flow is the least sensitive to inflow conditions) and are shown in Fig. 2. All through this paper, an overbar denotes time-averaging surrogating for Reynolds-averaging at a specific location, and the instantaneous velocity is thus decomposed into this Reynolds average and a turbulent perturbation following, for example, $u = \overline{u} + u'$. The mean wind profiles match reasonably well with the wind tunnel experiment results, and with Fluent results despite the much higher resolution for the Fluent simulations inside the canopy due to its conforming mesh and refinement capability. Surprisingly, the match for the round roof is better than for the flat roof, with the pitched roof in between in terms of model performance. For the velocity variance, our LES shows similar trends to the wind tunnel measurements but the absolute values are generally larger, except for the flat roof case. Fluent results match the wind tunnel better for the flat and pitched roof, but not for the round roof. In general, the higher resolution in our LES does not improve the agreement with the experiments, indicating that grid refinement is not necessarily an easy-solution for reducing model errors. For round and pitched roofs, the flow is sensitive to the separation point as discussed before; that point is expected to be Re-independent only for flows over flat roofs where it would occur at the leeward corner of the building (Aynsley 1999; Temmerman et al. 2003). The comparable match between LES and wind tunnel results for the non-flat cases, relative to

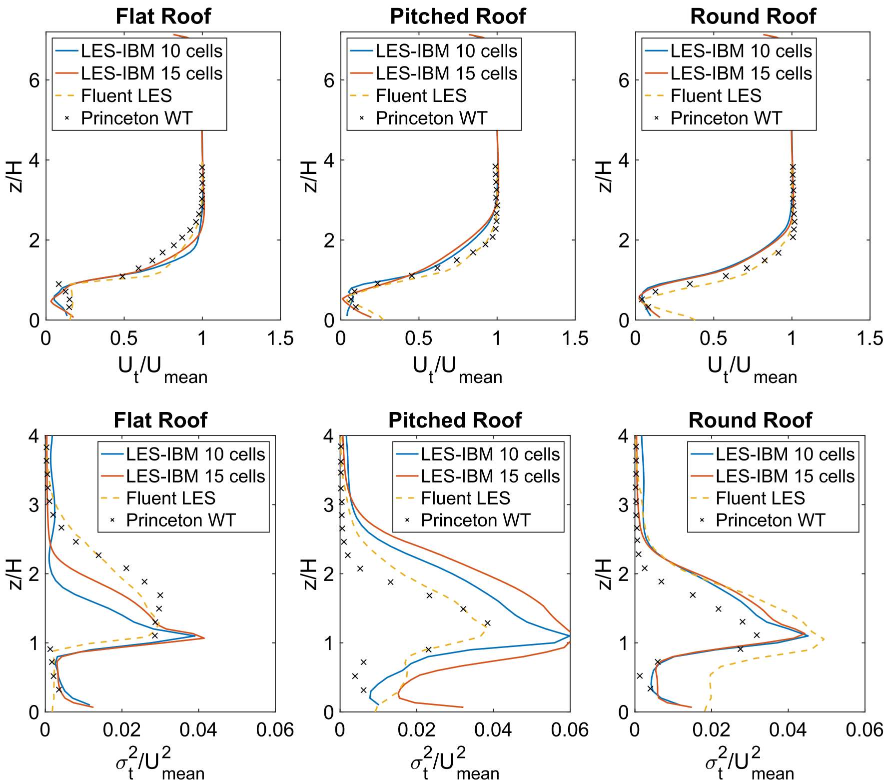

Fig. 2 Mean (first row) and variance (second row) of the velocity in the middle of canopy #6 for three roof geometries

Table 3 Comparison of the LES (of this paper) simulated statistics to the meteorological tower measurements and the results of Giometto et al. (2017), for the cases they simulated without trees

Parameter	Tower		LES (Giometto)	LES (this paper)	SL
	Winter	Summer	No trees	No trees	
σ_u/u_*	2.310	2.323	2.35	2.154	2.2
σ_w/u_*	1.206	1.209	1.16	1.165	1.25
r_{uw}	−0.366	−0.365	−0.364	−0.384	−0.360
SK_w	0.142	0.204	0.177	0.115	
TKE/MKE	0.155	0.174	0.071	0.071	

SL here represents the surface layer neutral limits at the height of the measurements (Panofsky and Dutton 1984)

the flat roof, is thus somewhat positively surprising. The results also become increasingly sensitive to the ability of the simulation to match inflow conditions (mean and turbulence) as the height above the ground increases, which explains the noticeably better match of our LES with wind tunnel data at heights < 1.5 H.

To evaluate the code for even more realistic setups, we also compared the simulated turbulence statistics to the tower measurements in Vancouver (Table 3), mimicking the setup

Table 4 Simulation setup parameters for the 4 selected city neighborhoods

	$L_x \times L_y \times L_z$ (m^3)	$N_x \times N_y \times N_z$	ETT (s)	Warm-up Time (ETT)	Averaging period (ETT)
S_{Bal}	590 × 443 × 385	160 × 128 × 108	41.6	173	87
S_{Bos}	1024 × 864 × 576	256 × 216 × 144	57.0	175	105
S_{OKC}	770 × 770 × 325	256 × 256 × 108	26.4	153	69
S_{Van}	280 × 250 × 72	256 × 256 × 72	6.7	179	90

in Giometto et al. (2017). The simulation domain size is $L_x \times L_y \times Lz = 940 \times 620 \times 192$ (m^3), with the number of grids $N_x \times N_y \times N_z = 250 \times 160 \times 50$ (notice that this domain is different from the the area selected later for simulations in the city S_{van} and for flow analysis). The wind approaches from the southwest direction. Here, we used a lower resolution compared to that in Giometto et al. (2017), but the code performance remains very similar to that original study for aggregate turbulent statistics. This is not entirely surprising since the code used by Giometto et al. (2017) is very similar to the present one (except for the smoothing to treat the Gibbs phenomenon). Overall, these comparisons show the ability of the LES code to reproduce the flow over realistic geometries with reasonable accuracy, including the vertical trends in the mean wind and variance that are essential to capture since we will use a combination of these quantities to analyze wind extremes and address the research questions. It should also be stressed that our analyses will focus on how urban geometry controls the location of gust and stagnation zones, and therefore our findings and conclusions are not highly sensitive to simulations errors at individual points. Therefore, we will not delve further into the code performance analysis and shift our focus to the flow physics.

2.4 Simulation Set-Up

LES was conducted over the 4 cities using their DSM data. The simulations are first warmed up for over 150 eddy turnover times. Subsequently, we simulated each neighborhood for about 70 eddy turnovers or more to collect flow statistics. We then checked that the total kinetic energy averaged over the domain varies by less than 2% of its running value at the end of this averaging period. The eddy turnover time was estimated as ETT $= h_{mean}/u_*$. Important experimental parameters are shown in Table 4. The domains are high enough ($\sim 10h_{mean}$) to minimize the impact of the top boundaries (Zahn and Bou-Zeid 2024) and minimize blockage effect. As previously mentioned, we use periodic boundary conditions in both streamwise and lateral directions, implying the the simulations are over infinite repetitions of identical canopies. While this is not an exact replica of the inflow for real neighborhoods, it does not impact our conclusions since we do not seek specific information about these neighborhoods, but rather a general association of geometry and gust and stagnation zones.

For real urban canopies, as argued earlier, it is not computationally feasible to require that each facet of each structure be resolved by $\approx$ 8 grid points (as recommended for our code by Tseng et al. (2006)). For the present simulations, we used the highest number of grid points that were practically computable (simulations not requiring more than $\sim$ 2 weeks to complete on a supercomputer), and most of the large and critical structures (e.g., the tall buildings that tend to also be wide) are well-resolved. An illustration for the mesh design is included in Online Resource 3.

3 Characterizing the Mean and Variability of the Flow

3.1 Selecting the Indicators for Gust and Stagnation Extremes

The complex urban surface modulates the spatio-temporal variability inside and above the canopy. Therefore, we are interested in how to quantify that variability, and specifically what metrics could be used to characterize both the extreme high winds leading to gust zones and the extreme low winds leading to stagnation zones. There are multiple ways to characterize the gusts at a specific location. The maximum wind velocity is a commonly used gust index (Monahan and Armendariz 1971; Wieringa 1973; Ahmad et al. 2017; Verkaik 2000). But since the statistics of the maximum are usually difficult to converge, a practical alternative indicator for extreme high winds is a percentile with specified exceedance frequency, e.g., the 99 percentile (Ikegaya et al. 2017; Wang et al. 2022; Wang and Okaze 2023). These metrics are useful for analysis of the safety level and building load requirements. However, to measure a specific percentile value, complete data at all points in time and space are needed. Storage of such raw LES time-series at each point in space remains memory intensive. In addition, for wide application of such analyses over multiple whole cities, the LES computations can become impractically expensive and Reynolds-averaged Navier Stokes (RANS) might be a more practical CFD approach. RANS does not simulate instantaneous velocities and would not be able to provide these metrics.

An alternative would be to define the gust and stagnation zones based on some statistical properties of the velocity that are easy to compute from the LES on-the-fly. One plausible option is to base these analyses on some statistic such as $\widetilde{M} + nM_{rms}$, where $M = \sqrt{u^2 + v^2 + w^2}$ is the total velocity, $\widetilde{M}$ is the magnitude of the mean velocity vector, and is calculated as $\widetilde{M} = \sqrt{\overline{u}^2 + \overline{v}^2 + \overline{w}^2}$, and M_{rms} is the root mean squared velocity and in the present paper is computed from the temporal variances of the three components as $M_{rms} = \sqrt{\sigma_u^2 + \sigma_v^2 + \sigma_w^2}$ (He and Song 1999). This metric can be defined independently of the type of the probability density function (PDF) for the velocity. However, computing associated exceedance probability (the complementary cumulative distribution function, which is equal to 1− the cumulative distribution function) does require knowledge of the probability distribution type. A specific version of such a metric that we will investigate here is $\widetilde{M} + 3M_{rms}$. The probability distribution of wind speeds is controlled by complex dynamics that contribute to its variation in time and space. Instantaneous wind velocity components over shorter periods can be described as a Gaussian random process (Nfaoui et al. 2004; Llaguno-Munitxa et al. 2017), although they typically have fatter tails. (See Online Resource 4 for the PDFs of each velocity component at 2 randomly selected locations in the canopy). The sum of squared independent variables, each following a Gaussian distribution, adheres to a generalized chi-square distribution; this had been shown to apply reasonably-well to the three velocity components despite their interdependence (Allouche et al. 2021). The square root of the generalized chi-square distribution results in the Nakagami distribution. However, the main goal here is to find regions with the highest or lowest winds, and thus the exact probability distribution model and the exact value of the exceedance probability associated with $+3M_{rms}$ do not impact these spatial analyses or our conclusions. Figure 3 compares the maximum wind velocity over one hour to $\widetilde{M} + 3M_{rms}$ in S_{Bal}, over a horizontal plane at pedestrian level (note here that all velocities shown in the figures are normalized by u_*). The two indicators show similar patterns, but the M_{max} is more random and discontinuous in space. This indicates that a high value of $\widetilde{M} + 3M_{rms}$ (or a similar statistic like $\widetilde{M} + 2M_{rms}$

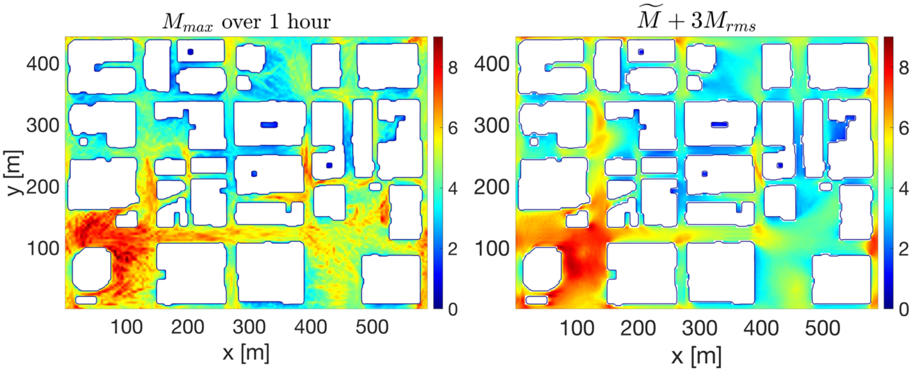

Fig. 3 Comparison of the maximum wind velocity M_{max} to $\widetilde{M} + 3M_{rms}$ in S_{Bal} at the pedestrian level $\sim$ 1.8m (the first grid node above the ground)

or $\widetilde{M} + 4M_{rms}$) is a more practical (than the max) and useful indicator for delineating zones with elevated extreme gust probability.

Similar concepts apply for characterizing the stagnation zones. One candidate is $|M|_{min}$, but it can be near 0 everywhere if we run the simulation for a long enough period. $\widetilde{M} - 3M_{rms}$ is also ill-suited since it will be negative when its minima indicate zones of low mean wind but high variance; and, if it is near zero, it may indicate zones where $\widetilde{M} = 3M_{rms}$, both of which may be large and can in fact ventilate the canyon quite efficiently. What is required here to characterize stagnation is not a measure of the weakest flow, but rather a measure of the weakest maximum possible ventilation events. To that end, we will adopt a low $\widetilde{M} + 3M_{rms}$ value as the indicator for the stagnation zones. These zones will have low values for both $\widetilde{M}$ and $3M_{rms}$, indicating the weakest gustiness and potentially also identifying the centers of recirculating motions. Such zones will rarely experience significant ventilation events, thus preventing the pollution and heat from being advected or dispersed.

Figure 4 displays horizontal, streamwise-vertical, and lateral-vertical slices of $\widetilde{M}+3M_{rms}$. Gusty zones are in red/orange and stagnation zones are in blue, according to our selected indicators. In Figs. 3 and 4, the spatial variation of $\widetilde{M}+3M_{rms}$ is visibly related to the building geometries, as expected. For example, there exists lower wind zones behind large building blocks, and $\widetilde{M} + 3M_{rms}$ is significantly larger around the tallest building in this domain (the building in the left bottom corner, for example). More variability can be noted inside the urban canopy.

The first row of Fig. 5 shows the ‘highest’ (gust) and ‘lowest’ (stagnation) wind zones in S_{Bal}, using $\widetilde{M}$, M_{rms} and $\widetilde{M} + 3M_{rms}$ separately to examine if the variability is driven by the mean or the rms. The color map here represents percentiles over the plane, with points with a wind velocity higher than the 75^{th} percentile value of the horizontal plane depicted in orange/yellow/green colors. Those with a lower wind velocity (<25 percentile in the horizontal plane) are in different shades of blue, while the values in between those percentiles are in white. The average wind ($\widetilde{M}$) and the variation in time (M_{rms}) contribute differently to $\widetilde{M} + 3M_{rms}$. Taking the high wind zones at the left bottom corner of the domain as an example, $\widetilde{M}$ mainly contributes to the high winds on the lateral sides of the tallest building, while M_{rms} is the cause of the high winds at the pedestrian level behind that building. In this study, we are only focused on the extreme winds as represented by $\widetilde{M} + 3M_{rms}$, but the results indicate that the maxima of this criterion are controlled more prominently by M_{rms} than by $\widetilde{M}$. For the minima, both M_{rms} and $\widetilde{M}$ need to be low to prevent ventilation and

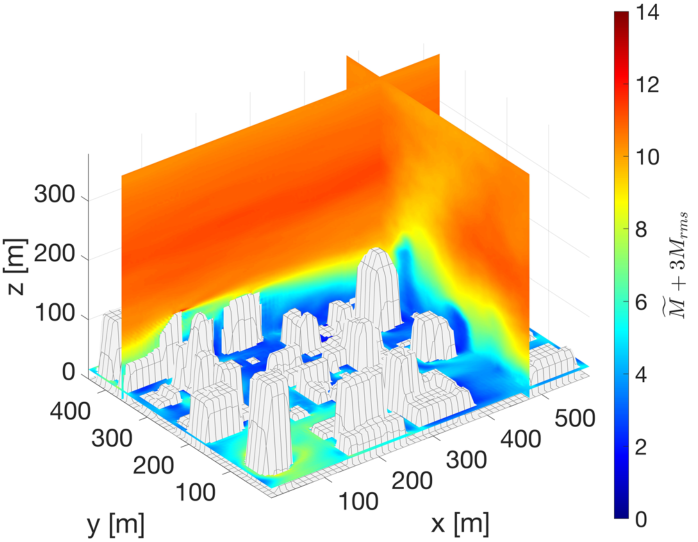

Fig. 4 Slices of $\widetilde{M}+3M_{rms}$ in S_{Bal}. The 3 slices shown here are located at (1) z = 16 m, (2) x = 478 m, (3) y = 362 m

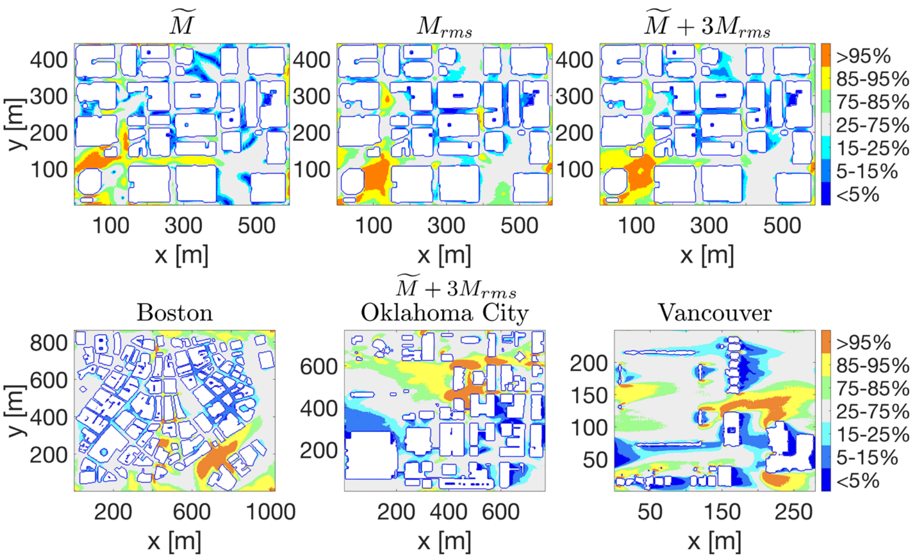

Fig. 5 The first row: comparison of the 'highest' and 'lowest' wind zones for $\widetilde{M}$, M_{rms} and $\widetilde{M}+3M_{rms}$ at the pedestrian level in S_{Bal}. The second row: Comparison of the 'highest' and 'lowest' wind zones represented by $\widetilde{M}+3M_{rms}$ for S_{Bos}, S_{OKC} and S_{Van}

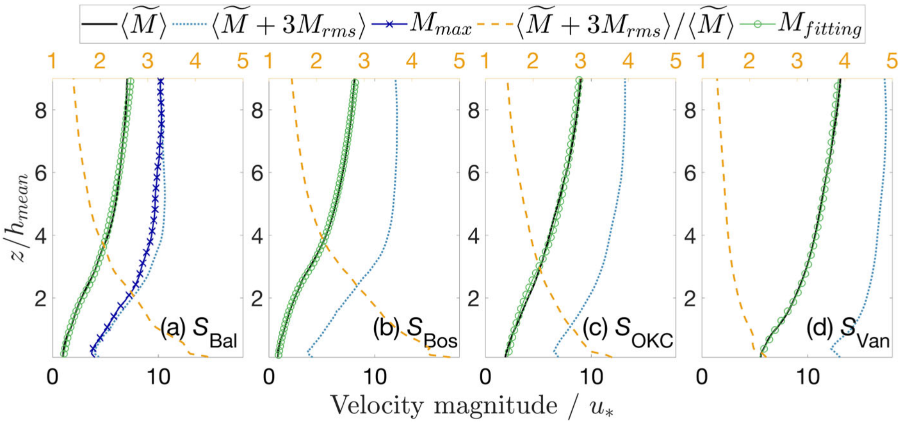

Fig. 6 Mean wind and gust profiles for the 4 city neighborhoods. The $\langle\cdot\rangle$ represents the value averaged over a single x–y plane. The top abscissa axis is for the normalized values $(\widetilde{M} + 3M_{rms})/\widetilde{M}$

produce stagnation zones. To ensure that the choice of the factor in front of M_{rms} (here n=3) does not alter our conclusions, a plot for the 'highest' and 'lowest' wind zones represented by $\widetilde{M} + 2M_{rms}$ and $\widetilde{M} + 4M_{rms}$ are included in Appendix 2; while the magnitudes differ, the overall spatial trends and identified gust and stagnation locations are very similar. This illustrates the robustness of this approach and confirms that the exact threshold used does not modify our conclusions. The gust and stagnation zones for $\widetilde{M} + 3M_{rms}$ are also plotted for the other 3 cities in the second row of Fig. 5. The wind patterns over other cities show a similar regularity.

3.2 Vertical Profiles of Mean and Extreme Winds Over the Different Cities

To further characterize the extreme winds and their vertical variability, we compared the profile of $\widetilde{M}+3M_{rms}$ (the light blue dotted lines) to that of the average wind (the black solid lines) (Fig. 6). Spatial averaging over the horizontal planes is done over the fluid volume only (intrinsic averaging, Schmid et al. (2019)). We fitted the mean wind profile using an exponential-logarithmic law (lime green lines with dot markers). The inflection point z_e in the exponential-logarithmic wind profile (where the curvature and the sign of the first gradient change) marks the transition between two different regimes of the wind speed profile. It is assumed that below z_e, the fitting profile follows the exponential law (Eq. 3), while above z_e it follows the logarithmic law (Eq. 4):

$$u = U_{ze}\exp\left(a\left(\frac{z}{z_e} - 1\right)\right), \tag{3}$$

$$\frac{u}{u_*} = \frac{1}{\kappa}ln\left(\frac{z-d}{z_0}\right). \tag{4}$$

The fitting parameters are shown in Table 5. For S_{Bal} and S_{Bos}, where the buildings are generally taller, both the mean winds and $\widetilde{M}+3M_{rms}$ are lower than for S_{OKC} (under the same synoptic forcing since these results are normalized by u_*). The mean winds and $\widetilde{M}+3M_{rms}$ are obviously the highest in S_{Van}, which is characterized by low-rise 2-storey buildings. In contrast to the results of wind profiles over cuboids with identical heights, the inflection point

Table 5 The fitting parameters for the exp-log law profiles for the mean winds in the 4 neighborhoods

	S_{Bal}	S_{Bos}	S_{OKC}	S_{Van}
z_e/h_{mean}	2.10	2.87	2.96	1.46
U_{ze}/u_*	3.00	3.76	5.01	7.88
a	1.20	1.51	0.91	0.40
d/h_{mean}	0.64	1.61	1.33	0.29
z_0/h_{mean}	0.44	0.28	0.22	0.05

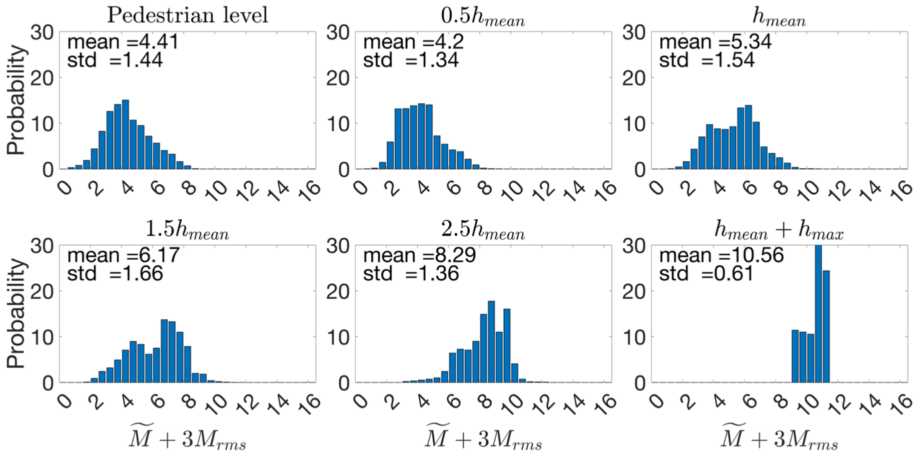

Fig. 7 Probability distribution for $\widetilde{M}+3M_{rms}$ at different vertical horizontal levels in S_{Bal}

z_e is higher than h_{mean} for all 4 neighborhoods, showing that the influence of the buildings extends above h_{mean} even when examining the horizontally averaged statistics. Moreover, the displacement height d/h_{mean} is larger than 1 for S_{Bos} and S_{OKC}, while it is typically less than one for uniform cuboids (Kanda et al. 2013) and ≈ 0.7 for vegetation canopies. Figure 6(a) for Baltimore also includes the profile of the maximum velocity over 1 h (dark blue cross markers), which matches the profile of $\widetilde{M}+3M_{rms}$ well, especially inside the urban canopy. It again confirms $\widetilde{M}+3M_{rms}$ is a good indicator for analyzing extreme high winds. The yellow dashed lines show $\widetilde{M}+3M_{rms}$ normalized by the mean wind. This normalized quantity decreases with height as the spatial variability of the flow decreases when the fraction of the horizontal plane covered by buildings drops.

While Fig. 6 depicted the mean profiles of $\widetilde{M}+3M_{rms}$, significant variability exists at each height. This variability is best illustrated using probability density functions (PDF) plots at selected heights, as shown in Fig. 7. At lower levels (below h_{mean}), the PDF is wide and positively skewed, which indicates that although the mean velocity is low close to the ground, the spatial variation can be large and favors extreme high wind values. Moving upward to $0.5h_{mean}$ and h_{mean}, the PDFs maintain a similar breadth as for the pedestrian level, but become more symmetrical. At $1.5h_{mean}$ and above, as buildings disappear, the mean of the PDF increases while its variability maintains a similar range; the distribution also becomes negatively skewed because the mean wind speed is here higher while there still exists low wind locations due to the influence of the highest buildings. At the height of $h_{mean}+h_{max}$, the normalized $\widetilde{M}+3M_{rms}$ is concentrated around 11, showing the vanishing impact of the buildings at one time the mean building height above the tallest building.

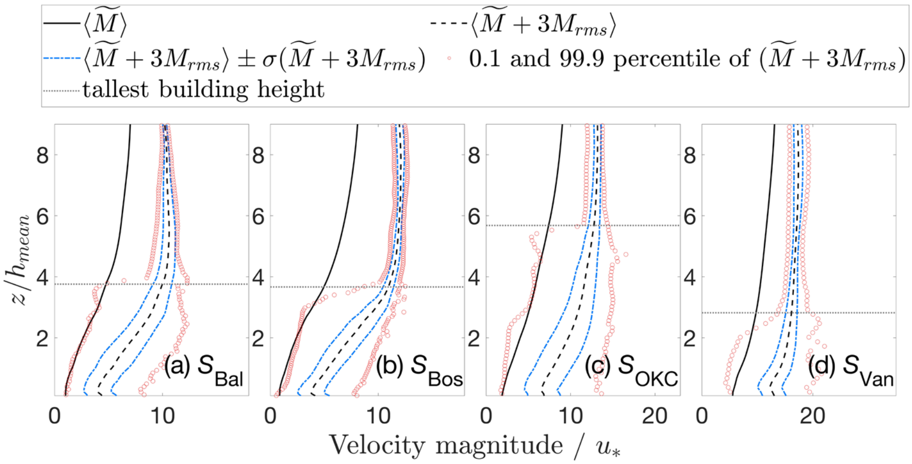

Fig. 8 Profiles for the mean wind $\widetilde{M}$, the wind gusts $\widetilde{M} + 3M_{rms}$, its ±1 standard deviation range, and its 0.1% / 99.9% over individual horizontal planes

The spatial variability of the extremes at a given height is further illustrated in Fig. 8, which depicts the mean, 0.1% / 99.9% percentile, and the spatial standard deviation profiles of $\widetilde{M} + 3M_{rms}$. The two blue dash-dotted lines show the one standard deviation interval of $\widetilde{M} + 3M_{rms}$; the variability becomes narrower as the height increases. The red circles represents the 0.1% / 99.9% percentile $\widetilde{M} + 3M_{rms}$ in a single x–y plane and are far from the intrinsic average of $\widetilde{M} + 3M_{rms}$. This underlines again the strong spatial variability of the $\widetilde{M} + 3M_{rms}$ fields that was depicted in previous figures. The gap is much larger inside the urban canopy, which shows that buildings can drastically reshape the wind fields, and that the analysis of urban geometries can be useful for understanding the wind variability. For S_{Bal}, S_{OKC} and S_{Van}, the maximum wind gusts of the whole domain occur around the tallest buildings, which are then exposed to higher forces that they need to be designed to withstand.

3.3 Stagnation Zones and Canyon Ventilation

While the minima of $\widetilde{M} + 3M_{rms}$, as we argued before, are a good indicator of stagnation zones; it is also useful to examine how urban ventilation varies with height more broadly. The air exchange rate (ACH), which is the volumetric air exchange per unit time, is a commonly used indicator for ventilation. Based on a folded-normal distribution model of the vertical velocity perturbations, ACH can be calculated to examine urban ventilation over a horizontal plane (Llaguno-Munitxa and Bou-Zeid 2018) following

$$ACH = \frac{A}{2}\left\langle \sqrt{\frac{2}{\pi}}\sigma_w \exp\left(-\frac{\overline{w}^2}{2\sigma_w^2}\right) - \overline{w}\,\mathrm{erf}\left(-\frac{\overline{w}}{\sqrt{2}\sigma_w}\right)\right\rangle : \qquad (5)$$

where erf is the error function, and as a reminder, w is the instantaneous local vertical velocity; an overbar denotes its local temporal average and the angled brackets denote spatial averaging over a horizontal plane. This model assumes that the vertical velocity is normally distributed (See Online Resource 4 where we show that, indeed, this is a reasonable assumption; also see Llaguno-Munitxa and Bou-Zeid (2018) and Lu et al. (2024)), and it was shown to give

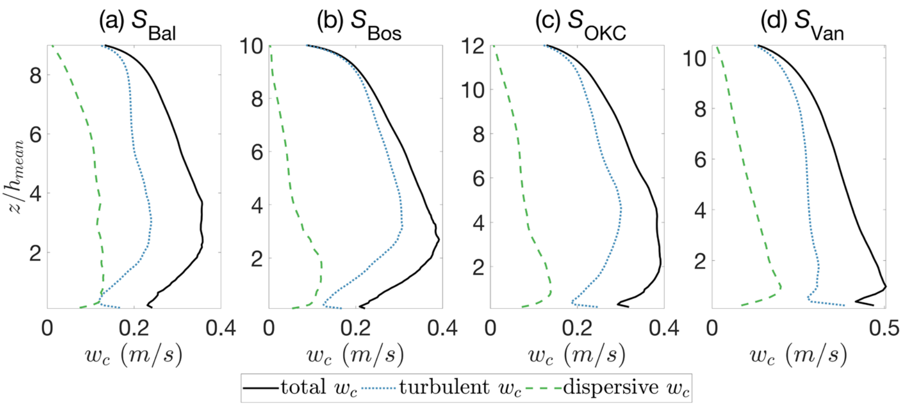

Fig. 9 The air exchange velocity and the turbulent and dispersive parts for the 4 neighborhoods

accurate estimates of urban ventilation (Llaguno-Munitxa and Bou-Zeid 2018). In addition, the dispersive component of the ACH can be calculated without any assumption on the probability distribution of the vertical velocity as:

$$ACH_{disp} = \frac{A}{2} \langle |\overline{w}| \rangle . \tag{6}$$

The turbulent ACH can then be calculated as $ACH_{turb} = ACH - ACH_{disp}$.

Unlike $\widetilde{M} + 3M_{rms}$, ACH is calculated from the vertical velocity component w. Figure. 9 shows the profiles for the turbulent and dispersive parts, as well as the total ACH. These ACH values are normalized by the planar area of each city; therefore, they are akin to exchange velocities (w_c). The peak of the total ACH and the turbulent ACH occur around 2-4h_{mean} for $S_{\rm Bal}$, $S_{\rm Bos}$ and $S_{\rm OKC}$. However, for $S_{\rm Van}$ the maxima occur around h_{mean}, which shows that the generally low and sparsely distributed buildings in $S_{\rm Van}$ suppress the influence of the few taller buildings on the ACH. For $S_{\rm Bos}$, $S_{\rm OKC}$ and $S_{\rm Van}$, the dispersive contributions reach their peak $\sim h_{mean}$ (for $S_{\rm Bal}$, there is a plateau for ACH_{disp} at $1{\sim}5h_{mean}$) and are smaller compared to the turbulent ACH. Near h, these dispersive fractions are comparable to those reported by Li and Bou-Zeid (2019) for square regular cuboids and Akinlabi et al. (2022) for Boston, and mildly lower than those reported by Llaguno-Munitxa and Bou-Zeid (2018) for 2D ribs. However, it is notable that the dispersive fluxes continue to be significant at higher elevations than h due to the tall buildings, and also potentially due to the inhomogeneity of the roughness at the neighborhood scale that can lead to large secondary circulations. Comparing these 4 neighborhoods, when buildings are taller and denser, there tends to be a lower air exchange rate, as expected.

Comparing the colourmap for $\widetilde{M} + 3M_{rms}$ and the local exchange velocity $w_{c,l}$, calculated at 10 m as per equation 5 but without spatial averaging (Fig. 10), one can detect the similarity of the spatial features of the two quantities, particularly in areas of low magnitude that we postulate are stagnation zones. This demonstrates that low values of $\widetilde{M} + 3M_{rms}$ can indeed be used to delineate zones prone to stagnation. ACH tends to be high close to walls in the streamwise direction, underlining the high vertical air transport, but the total wind velocity M can be suppressed especially for areas at the leeward side of buildings. However, both variables can delineate the areas with the lowest ventilation, identified by the inverted pink triangles in Fig. 10.

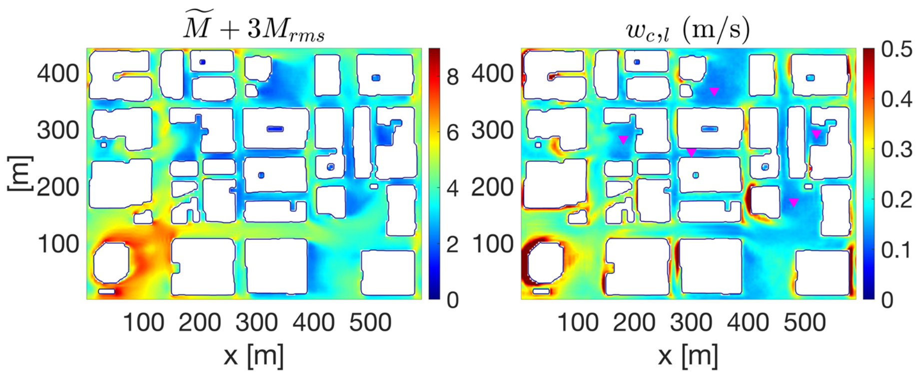

Fig. 10 Comparison of $\widetilde{M} + 3M_{rms}$ and $w_{c,l}$ in S_{Bal} at 10 m level. The triangular markers identify the stagnation zones determined by both variables

4 Geometric Determinants of Extreme Winds

Since the high and low wind extremes are intimately related to the surface geometry, as illustrated in the previous sections (e.g., the wind tends to be weaker behind large building blocks, while it can be extremely high around the isolated tallest building (Fig. 5)), in this section, we attempt to identify urban form parameters that can help predict gust and stagnation zones.

4.1 Plan and Frontal Area Fraction

The plan area fraction (λ_p) and the frontal area fraction (λ_f) are widely used parameters for characterizing the building density. The frontal area fraction is a parameter quantifying the total built area projected in the incoming wind direction (including all buildings, not just the ones at the front), it thus contains information about the building orientation and ability to impose a pressure drag on the flow. The plan area fraction encodes building density, and when computed at multiple levels, how that density varies with height. When the building height distribution is uniform, λ_p then becomes a single value. In this section λ_p and λ_f are defined as

$$\lambda_p(z) = A_p(z)/A_T \; : \tag{7}$$

$$\lambda_f(z) = \int_z^{z_i} \mathrm{d}A_f(\zeta)\mathrm{d}\zeta/A_T, \tag{8}$$

where A_T is the total domain area; $A_p(z)$ is the area covered by buildings at height z; and $\int_z^{z_i} \mathrm{d}A_f(\zeta)\mathrm{d}\zeta$ is the projection area of all buildings between z and z_i in the wind direction (Oke et al. 2017; Li et al. 2020a). The frontal area as computed here is thus an integral from the top of the domain to the level of interest. The rationale for this formulation is that the main momentum source is above the canopy, and this integral thus indicates the total area that extracted momentum from the flow down till the height of interest. (The vertical structure of λ_p and λ_f are shown in Online Resource 5).

The two fractions λ_f and λ_p are not independent as they are both related to building density. However, they are not perfectly linearly correlated, as shown in Fig. 11. For example, two

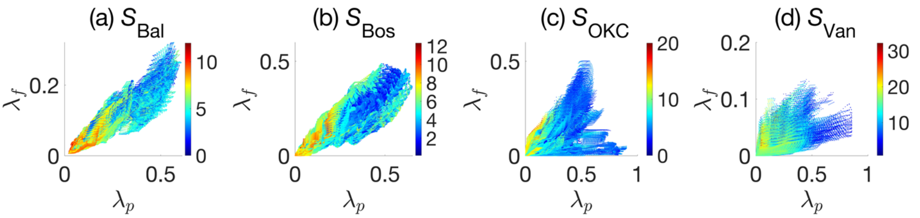

Fig. 11 λ_f versus λ_p for the 4 neighborhoods between the ground level and $2h_{mean}$. The colors represent the normalized $\widetilde{M} + 3M_{rms}$

buildings with the same cross stream width but highly different streamwise depths may have the same projection area in the wind direction (λ_f), but the building that is longer in the streamwise direction will result in a much larger plan area (λ_p). The data points in Fig. 11 are coloured by $\widetilde{M} + 3M_{rms}$ to inform on how these two parameters jointly control extreme winds. Here, λ_f and λ_p are calculated for each $8h_{mean} \times 6h_{mean}$ sub-area in the upwind direction relative to the grid point at which $\widetilde{M} + 3M_{rms}$ is recorded. We tried different sub-area dimensions and use $8h_{mean} \times 6h_{mean}$ for further analysis since it displayed the most consistent patterns. With this sub-area dimension that captures the geometric impacts of a few blocks, Fig. 11 shows that $\widetilde{M} + 3M_{rms}$ generally decreases with both λ_f and λ_p as expected physically. Alternative areas spanning $7h_{mean} \times 5h_{mean}$ and $9h_{mean} \times 7h_{mean}$ were also tested, showing similar trends of $\widetilde{M} + 3M_{rms}$ for the geometric features discussed here. In Fig. 11, within the dense lower part of the canopy sublayer, $\widetilde{M} + 3M_{rms}$ tends to be high only when both λ_f and λ_p are small, which indicates a relatively open area to which high speed air can easily penetrate from aloft. On the other hand, while stagnation zones with low $\widetilde{M} + 3M_{rms}$ are induced by both fractions being high, they can also occur when λ_p is high, regardless of λ_f.

Since the previous results show that a high wind ($\widetilde{M} + 3M_{rms}$) can be attributed to the joint effect of a small λ_f and a small λ_p, we investigate whether the sum of these two fractions can encode their joint effect. This sum represents the ratio of the total area directly exposed to incoming wind (the front and roof area) to the total subdomain area ($8h_{mean} \times 6h_{mean}$). The grey dots in Fig. 12 show that $\widetilde{M} + 3M_{rms}$ generally decreases with $\lambda_p + \lambda_f$. However, for a given value of $\lambda_p + \lambda_f$, there is still a wide range of variability. These fractions are thus necessary but not sufficient parameters to explain urban wind extremes.

If we just focus on the extreme high wind zones, we find that the 95th percentile values of $\widetilde{M} + 3M_{rms}$ have a clear decreasing trend against $\lambda_p + \lambda_f$ (yellow triangles), and the highest $\widetilde{M} + 3M_{rms}$ in space can only appear where $\lambda_p + \lambda_f$ is small. Similarly for the stagnation zones, the lowest (5th percentile) $\widetilde{M} + 3M_{rms}$ tend to appear where $\lambda_p + \lambda_f$ is large. The largest $\lambda_p + \lambda_f$ values are mostly found near the ground where the incoming wind is blocked by tall wide buildings. But it is not a strict necessity, the figure shows that the purple plus signs have a plateau for S_{Bal} and S_{OKC}, which means that stagnation zones can also be found at intermediate values of $\lambda_p + \lambda_f$. Thus, upwind blockage by dense tall buildings is not the only favorable geometry for air stagnation.

4.2 Sky View Factor

Another useful parameter in describing the building geometry is the sky view factor (SVF) (Lindberg et al. 2018), which represents the ratio of the visible sky to hemisphere centered

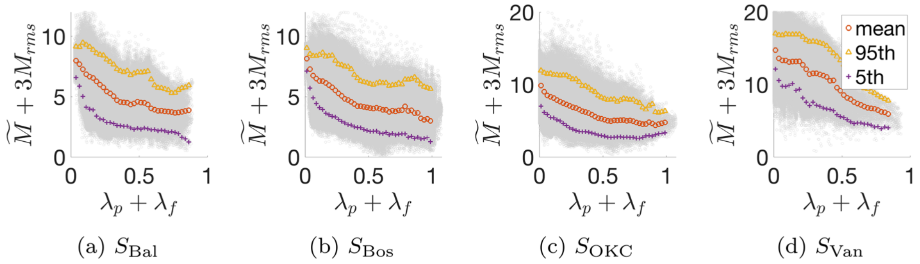

Fig. 12 $\widetilde{M} + 3M_{rms}$ versus $\lambda_p + \lambda_f$ for all grids between the ground level and $2h_{mean}$. The circles (red) represent the mean, the triangles (yellow) indicate the 95th percentile values, and the plus signs (purple) denote the 5th percentile values for each 0.025 $\lambda_p + \lambda_f$ bin. (The mean, 5th, and 95th percentile values are not shown for bins with fewer than 100 grid points)

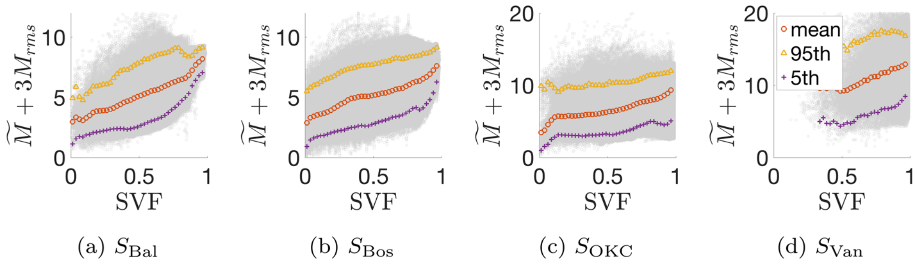

Fig. 13 $\widetilde{M} + 3M_{rms}$ versus the SVF for all grids between the ground level and $2h_{mean}$ in **a** S_{Bal}, **b** S_{Bos}, **c** S_{OKC} and **d** S_{Van}. The circles (red) represent the mean, the triangles (yellow) indicate the 95th percentile values, and the plus signs (purple) denote the 5th percentile values for each 0.025 SVF bins. The mean / 5th and 95th percentile values are not shown for bins with fewer than 100 grids

at a location. Here, we use this 3D SVF, which has been relatively less studied in its effects on the real urban winds, to discover its effect on realistic urban flows (Feng et al. 2021). The SVF is a good measure of the "depth" of a point below the overlying air flow. Inside the urban canopy, a small SVF means that the location is closely surrounded by tall buildings. SVF also contains information about the building density, similar to λ_p. However, our tests show that SVF is not simplistically correlated with λ_p or λ_f. Here, the SVF is calculated using the UMEP, a plugin in QGIS (Lindberg et al. 2019). A continuous SVF calculated for OKC is shown in Appendix 3. An appealing attribute of SVF is that it can be calculated locally at every point, while λ_p and λ_f need some area over which they are defined (e.g., $8h_{mean} \times 6h_{mean}$ in the present study). Figure 13 shows that $\widetilde{M} + 3M_{rms}$ tends to increase with the SVF for the 4 neighborhoods, as expected when the point is more connected fluidically to the sky. Similar to $\lambda_p + \lambda_f$, for a fixed SVF, there is a wide range of possible $\widetilde{M} + 3M_{rms}$, but it is clear that there is higher probability of extreme high winds at locations where SVF is large. (To compare the trends in the four cities, the mean of each bins (the red markers) in Fig. 12 and Fig. 13 are shown in one plot in Online Resource 6). This analysis is useful since it shows that SVF contains pertinent fluid mechanics information, while in the past it has mainly been used for characterizing radiative exchanges.

5 Conclusions

In this study, we aimed to investigate the flow over real cities, with a focus on identifying the best fluid dynamic indicators characterizing gust and stagnation zones, examining the vertical variability of mean and extreme wind statistics in different cities, and uncovering key urban geometric attributes that can help explain extreme high or low wind zones. To these ends, LES with bluff bodies resolved by an immersed boundary method was applied for simulating the wind fields in urban terrain. Our LES code shows good performance for simulating the mean wind and captures the vertical trends for the mean and variance of the velocity well for different roof shapes, in comparison to wind tunnel measurements. The comparison to meteorological tower measurements in a Vancouver neighborhood also shows that our code can capture the turbulence statistics at a single point in real cities. For the broader analyses, four neighborhoods distinct in their building morphologies were simulated.

The findings allowed us to answer the three questions that motivated this study, as listed in the introduction. $\widetilde{M} + 3M_{rms}$ was shown to be a useful indicator for the extremes of the statistical distributions of wind speeds. Its high values are good surrogates for elevated M_{max}, and thus good indicators of gust risk. In addition, a low $\widetilde{M} + 3M_{rms}$ value indicates poor ventilation and corresponds to high probability of stagnation, as confirmed by its spatial patterns matching those of low air exchange rates. The mean wind, as well as $\widetilde{M} + 3M_{rms}$, are affected by the urban geometries, especially by the large bluff bodies or tall buildings.

Comparing the simulation results in the 4 neighborhoods, we found that with denser and taller buildings, both mean winds and $\widetilde{M} + 3M_{rms}$ averaged horizontally tend to be lower under the same synoptic forcing. Complex surface geometries exacerbate the spatio-temporal variability in the roughness sublayer. The influence of buildings can extend well above the canopy sublayer, but the geometry-induced variability becomes much smaller above the highest buildings.

Many building geometry parameters can be important for the extreme winds, including the building height, height variability, building footprints and density, building arrangement and the angle with the wind above the canopy. In this study, we investigated three critical parameters that are expected to explain a large fraction of the variability: the plan and frontal area fractions and the sky view factor. These three parameters are not only dependent on the building density, but also contain information about the street width and openness. Among them λ_f and SVF are related to the building height and orientation, while SVF is additionally related to the distance from the wall. $\widetilde{M} + 3M_{rms}$ generally decreases with $\lambda_p + \lambda_f$ and increases with SVF, although there is a large range of variability that remains unexplained by these parameters.

This study brings to light at least as many questions as it answers. First, the performance of the LES, while adequate for the analyses of this paper, was confounding with better performance over complex rather than flat roofs. There is clearly a need for more studies focusing on the impact of urban geometry on LES performance, and on improving urban LES skills more generally. Furthermore, while the two urban densities and the SVF clearly explained part of the variability of winds, there remains a lot of unexplained variability that hints at other important factors needed to explain the extremes, like street orientation and tortuosity, among others. Despite these constraints, this study elucidates the importance of key urban geometric parameters in understanding wind extrema, and establishes metrics that can be used to detect gust and stagnation zones, providing insight for studying the role of other geometric features for future works. Developing more accurate and general models for wind extremes might benefit from a machine learning approach where the gust and stagnation zones are predicted based on a large number of input geometric parameters, and the most informative of these parameters are also identified (as done by Gerges et al. (2024), for example, for urban air quality).

Appendix 1 Implementation of the Time Advancement in the LES Model

For the numerical solution, Eq. 2 is rewritten as:

$$\frac{\partial u_i}{\partial t} + \frac{\partial p^*}{\partial x_i} - B_i = -u_j \left(\frac{\partial u_i}{\partial x_j} - \frac{\partial u_j}{\partial x_i} \right) - \frac{\partial \tau_{ij}}{\partial x_j} + F_i, \tag{9}$$

and the time advancement is split into 2 steps. The first step accounts for all the terms on the right hand side (RHS) of this equation at the current time step n, as well as the contribution to the second-order Adam-Bashforth (AB2) time advancement scheme from the pressure field at the previous time step $n-1$, to obtain an intermediate velocity u_i^* from:

$$\frac{u_i^* - u_i^n}{\Delta t} = \frac{3}{2} RHS_i^n - \frac{1}{2} RHS_i^{n-1} + \frac{1}{2} \frac{\partial p^{n-1}}{\partial x_i}. \tag{10}$$

Then, a Poisson solver is used to update the pressure field using the u_i^* field in which the velocity is now also forced to zero inside the bluff bodies. The Poisson equation is obtained by taking the divergence of Eq. 2, and then imposing the divergence free condition in that equation following $\partial u_i^{n+1}/\partial x_i = \partial B_i/\partial x_i = 0$. The updated pressure is then used in the second part of the time step to account for the contribution to the AB2 time advancement from the pressure field at the current time step n, as well as the influence of the IBM force (0 force in the fluid domain, and calculated to produce zero velocity inside the buildings) following:

$$\frac{u_i^{n+1} - u_i^*}{\Delta t} = -\frac{3}{2} \frac{\partial p^n}{\partial x_i} + B_i. \tag{11}$$

Appendix 2 Selection of the threshold for the instantaneous wind extremes

Compared to the extreme wind zones for $\widetilde{M} + 3M_{rms}$ shown in Fig. 5, Fig. 14 shows that the selection of different thresholds yields similar trends and does not modify our conclusions.

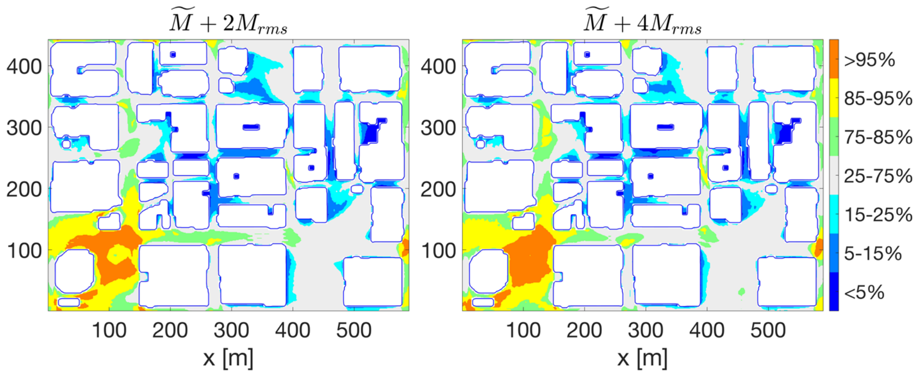

Fig. 14 Comparison of the 'highest' and 'lowest' wind zones for $\widetilde{M}+2M_{rms}$ and $\widetilde{M}+4M_{rms}$ at the pedestrian level in S_{Bal}

Appendix 3 Map of SVF at ground level

Figure 15 depicts the SVF at each point at ground level, showing how it varies in space.

Fig. 15 A continuous sky view factor plot for OKC calculated at the ground level

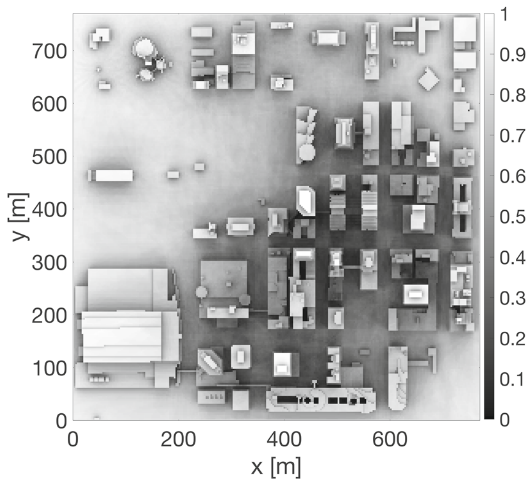

Supplementary Information The online version contains supplementary material available at https://doi.org/10.1007/s10546-025-00899-9.

Acknowledgements This work was supported by the Army Research Office under contract W911NF-20-1-0216, and by Samsung Advanced Institute of Technology. The LES simulations are conducted on the Cheyenne supercomputer of the National Center for Atmospheric Research (doi:10.5065/D6RX99HX) under project UPRI0021.

Author Contributions J.W. organized all the data, conducted the analysis, prepared the figures and wrote the main manuscript text. Q.L. and M.G. provided part of the data. E.B. provided overall guidance for the research and gave important suggestions on the study design and methods. All authors reviewed the manuscript.

Data Availability The data generated by the LES and used in this study are available at https://doi.org/10.5281/zenodo.14676236.

Declarations

Conflict of interest Jing Wang reports financial support, administrative support, equipment, drugs, or supplies, and travel were provided by Princeton University. Maider Llaguno Munitxa reports financial support, administrative support, and equipment, drugs, or supplies were provided by Catholic University of Louvain. Qi Li reports financial support, administrative support, and equipment, drugs, or supplies were provided by Cornell University. Marco Giometto reports financial support, administrative support, and equipment, drugs, or supplies were provided by Columbia University. Elie Bou-Zeid reports financial support, administrative support, equipment, drugs, or supplies, and travel were provided by Princeton University. Marco Giometto reports a relationship with Amazon.com Inc that includes: employment. Elie Bou-Zeid reports a relationship with Southwest Urban Corridor Integrated Field Laboratory that includes: board membership and consulting or advisory. If there are other authors, they declare that they have no known competing financial interests or personal relationships that could have appeared to influence the work reported in this paper.

References

Ahmad NH, Inagakia A, Kanda M, Onodera N, Aoki T (2017) Simulation of the gust index in an urban area using the lattice Boltzmann method. Boundary-Layer Meteorol 163(1):447–467. https://doi.org/10.1007/s10546-017-0233-6

Akinlabi E, Maronga B, Giometto M, Li D (2022) Dispersive fluxes within and over a real urban canopy: a large-eddy simulation study. Boundary-Layer Meteorol. https://doi.org/10.1007/s10546-022-00725-6

Allouche M, Katul GG, Fuentes JD, Bou-Zeid E (2021) Probability law of turbulent kinetic energy in the atmospheric surface layer. Phys Rev Fluids. https://doi.org/10.1103/physrevfluids.6.074601

Allouche M, Bou-Zeid E, Iipponen J (2023) The influence of synoptic wind on <scp>land-sea</scp> breezes. Q J R Meteorol Soc 149(757):3198–3219. https://doi.org/10.1002/qj.4552

Anderson W, Li Q, Bou-Zeid E (2015) Numerical simulation of flow over urban-like topographies and evaluation of turbulence temporal attributes. J Turbulence. https://doi.org/10.1080/14685248.2015.1031241

Angel S (2012) Planet of cities. Lincoln Institute of Land Policy Cambridge, MA

Arkon CA, Özkol Ü (2014) Effect of urban geometry on pedestrian-level wind velocity. Archit Sci Rev 57(1):4–19. https://doi.org/10.1080/00038628.2013.835709

Aynsley R (1999) Shape and flow: the essence of architectural aerodynamics. Archit Sci Rev 42(2):69–74. https://doi.org/10.1080/00038628.1999.9696854

Baklanov A, Sue G, Alexander M, Athanassiadou M (2009) Meteorological and air quality models for urban areas, vol 184. Springer, New York

Blocken B, Carmeliet J (2004) Pedestrian wind environment around buildings: literature review and practical examples. J Therm Envelope Build Sci 28(2):107–159. https://doi.org/10.1177/1097196304044396

Blocken B, Stathopoulos T, Van Beeck J (2016) Pedestrian-level wind conditions around buildings: review of wind-tunnel and cfd techniques and their accuracy for wind comfort assessment. Build Environ 100:50–81. https://doi.org/10.1016/j.buildenv.2016.02.004

Bou-Zeid E, Meneveau C, Parlange MB (2004) Large-eddy simulation of neutral atmospheric boundary layer flow over heterogeneous surfaces: Blending height and effective surface roughness. Water Resour Res. https://doi.org/10.1029/2003WR002475

Bou-Zeid E, Meneveau C, Parlange M (2005) A scale-dependent Lagrangian dynamic model for large eddy simulation of complex turbulent flows. Phys Fluids 17(2):025105. https://doi.org/10.1063/1.1839152

Bou-Zeid E, Overney J, Rogers BD, Parlange MB (2009) The effects of building representation and clustering in large-eddy simulations of flows in urban canopies. Boundary-Layer Meteorol 132:415–436. https://doi.org/10.1007/s10546-009-9410-6

Britter RE, Hanna SR (2003) Flow and dispersion in urban areas. Annu Rev Fluid Mech 35(1):469–496. https://doi.org/10.1146/annurev.fluid.35.101101.161147

Brown M, Lawson R, DeCroix D, Lee R (2001) Comparison of centerline velocity measurements obtained around 2d and 3d building arrays in a wind tunnel. In: International Society of Environmental Hydraulics Conf, Tempe, AZ

Chen F, Kusaka H, Bornstein R, Ching J, Grimmond C, Grossman-Clarke S, Loridan T, Manning K, Martilli A, Miao S (2011) The integrated wrf/urban modelling system: development, evaluation, and applications to urban environmental problems. Int J Climatol 31:273–288. https://doi.org/10.1002/joc.2158

Chester S, Meneveau C, Parlange MB (2007) Modeling turbulent flow over fractal trees with renormalized numerical simulation. J Comput Phys 225(1):427–448. https://doi.org/10.1016/j.jcp.2006.12.009

Coceal O, Belcher S (2004) A canopy model of mean winds through urban areas. Q J R Meteorol Soc 130(599):1349–1372

Coceal O, Dobre A, Thomas T, Belcher SE (2007) Structure of turbulent flow over regular arrays of cubical roughness. J Fluid Mech. https://doi.org/10.1017/S002211200700794X

Dagnew A, Bitsuamlak GT (2013) Computational evaluation of wind loads on buildings: a review. Wind Struct 16(6):629–660. https://doi.org/10.12989/was.2013.16.6.629

Day D, Jacobsen K, Passini R, Quillen S (2013) A study on accuracy and fidelity of terrain reconstruction after filtering dsms produced by aerial images and airborne lidar surveys. In: ASPRS 2013 Annual Conference, Baltimore, MD

Dodman D, Hayward B, Pelling M, Castan Broto V, Chow W, Chu E, Dawson R, Khirfan L, McPhearson T, Prakash A, Zheng Y, Ziervogel G (2022) Cities, settlements and key infrastructure. In: Pörtner HO, Roberts DC, Tignor M, Poloczanska ES, Mintenbeck K, Alegría A, Craig M, Langsdorf S, Löschke S, Möller V, Okem A, Rama B (eds) Climate Change 2022: Impacts, Adaptation and Vulnerability. Contribution of Working Group II to the Sixth Assessment Report of the Intergovernmental Panel on Climate Change, Cambridge University Press, Cambridge, UK and New York, USA, book section 6, pp 907–1040. https://doi.org/10.1017/9781009325844.008.907

Du Y, Mak CM (2018) Improving pedestrian level low wind velocity environment in high-density cities: a general framework and case study. Sustain Cities Soc 42:314–324. https://doi.org/10.1016/j.scs.2018.08.001

Feng W, Ding W, Fei M, Yang Y, Zou W, Wang L, Zhen M (2021) Effects of traditional block morphology on wind environment at the pedestrian level in cold regions of Xi'an, China. Environment, Development and Sustainability 23. https://doi.org/10.1007/s10668-020-00714-0

García-Sánchez C, Philips D, Gorlé C (2014) Quantifying inflow uncertainties for cfd simulations of the flow in downtown Oklahoma city. Build Environ 78:118–129. https://doi.org/10.1016/j.buildenv.2014.04.013

Gerges F, Llaguno-Munitxa M, Zondlo MA, Boufadel MC, Bou-Zeid E (2024) Weather and the city: machine learning for predicting and attributing fine scale air quality to meteorological and urban determinants. Environ Sci Technol 58(14):6313–6325. https://doi.org/10.1021/acs.est.4c00783

Giometto M, Christen A, Meneveau C, Fang J, Krafczyk M, Parlange M (2016) Spatial characteristics of roughness sublayer mean flow and turbulence over a realistic urban surface. Boundary-Layer Meteorol. https://doi.org/10.1007/s10546-016-0157-6

Giometto MG, Christen A, Egli PE, Schmid MF, Tooke R, Coops N, Parlange MB (2017) Effects of trees on mean wind, turbulence and momentum exchange within and above a real urban environment. Adv Water Resour 106:154–168. https://doi.org/10.1016/j.advwatres.2017.06.018

Glavovic B, Dawson R, Chow W, Garschagen M, Haasnoot M, Singh C, Thomas A (2022) Cross-chapter paper 2: Cities and settlements by the sea. In: Pörtner HO, Roberts DC, Tignor M, Poloczanska ES, Mintenbeck K, Alegría A, Craig M, Langsdorf S, Löschke S, Möller V, Okem A, Rama B (eds) Climate Change 2022: Impacts, Adaptation and Vulnerability. Contribution of Working Group II to the Sixth Assessment Report of the Intergovernmental Panel on Climate Change, Cambridge University Press, Cambridge, UK and New York, USA, book section Cross-Chapter Paper 2, pp 2163–2194. https://doi.org/10.1017/9781009325844.019.2163

Gopalan H, Heinz S, Stöllinger MK (2013) A unified rans-les model: computational development, accuracy and cost. J Comput Phys 249:249–274. https://doi.org/10.1016/j.jcp.2013.03.066

Goulart E Jr, N, Lavor V, Castro I, Santos JM, Xie ZT, (2018) Local and non-local effects of building arrangements on pollutant fluxes within the urban canopy. Build Environ. https://doi.org/10.1016/j.buildenv.2018.09.023

He J, Song CC (1999) Evaluation of pedestrian winds in urban area by numerical approach. J Wind Eng Ind Aerodyn 81(1):295–309. https://doi.org/10.1016/S0167-6105(99)00025-2

Hertwig D, Gough HL, Grimmond S, Barlow JF, Kent CW, Lin WE, Robins A, Hayden P (2019) Wake characteristics of tall buildings in a realistic urban canopy. Boundary-Layer Meteorol 172(2):239–270. https://doi.org/10.1007/s10546-019-00450-7

Huang J, Bou-Zeid E (2013) Turbulence and vertical fluxes in the stable atmospheric boundary layer. part i: a large-eddy simulation study. J Atmos Sci 70(6):1513–1527. https://doi.org/10.1175/JAS-D-12-0167.1

Hunt J, Poulton E, Mumford J (1976) The effects of wind on people; new criteria based on wind tunnel experiments. Build Environ 11(1):15–28. https://doi.org/10.1016/0360-1323(76)90015-9

Ikegaya N, Ikeda Y, Hagishima A, Tanimoto J (2017) Evaluation of rare velocity at a pedestrian level due to turbulence in a neutrally stable shear flow over simplified urban arrays. J Wind Eng Ind Aerodyn 171:137–147. https://doi.org/10.1016/j.jweia.2017.10.002

Kanda M, Moriwaki R, Kasamatsu F (2004) Large-eddy simulation of turbulent organized structures within and above explicitly resolved cube arrays. Boundary-Layer Meteorol 112:343–368

Kanda M, Inagaki A, Miyamoto T, Gryschka M, Raasch S (2013) A new aerodynamic parametrization for real urban surfaces. Boundary-Layer Meteorol. https://doi.org/10.1007/s10546-013-9818-x

Kawaminami T, Ikegaya N, Hagishima A, Tanimoto J (2018) Velocity and scalar concentrations with low occurrence frequencies within urban canopy regions in a neutrally stable shear flow over simplified urban arrays. J Wind Eng Ind Aerodyn 182:286–294. https://doi.org/10.1016/j.jweia.2018.09.024

Khaled M, Aly A, Elshaer A (2021) Computational efficiency of cfd modeling for building engineering: An empty domain study. J Build Eng 42(102):792. https://doi.org/10.1016/j.jobe.2021.102792

Kleissl J, Kumar V, Meneveau C, Parlange MB (2006) Numerical study of dynamic smagorinsky models in large-eddy simulation of the atmospheric boundary layer: validation in stable and unstable conditions. Water Resour Res. https://doi.org/10.1029/2005WR004685

Kubota T, Miura M, Tominaga Y, Mochida A (2008) Wind tunnel tests on the relationship between building density and pedestrian-level wind velocity: development of guidelines for realizing acceptable wind environment in residential neighborhoods. Build Environ 43(10):1699–1708. https://doi.org/10.1016/j.buildenv.2007.10.015

Kumar V, Kleissl J, Meneveau C, Parlange MB (2006) Large-eddy simulation of a diurnal cycle of the atmospheric boundary layer: atmospheric stability and scaling issues. Water Resour Res. https://doi.org/10.1029/2005WR004651

Kumar V, Svensson G, Holtslag A, Meneveau C, Parlange MB (2010) Impact of surface flux formulations and geostrophic forcing on large-eddy simulations of diurnal atmospheric boundary layer flow. J Appl Meteorol Climatol 49(7):1496–1516. https://doi.org/10.1175/2010JAMC2145.1

Kurppa M, Hellsten A, Auvinen M, Raasch S, Vesala T, Järvi L (2018) Ventilation and air quality in city blocks using large-eddy simulation-urban planning perspective. Atmosphere. https://doi.org/10.3390/atmos9020065

Lee S, Ham Y (2021) Probabilistic framework for assessing the vulnerability of power distribution infrastructures under extreme wind conditions. Sustain Cities Soc 65(102):587. https://doi.org/10.1016/j.scs.2020.102587

Li D, Bou-Zeid E (2013) Synergistic interactions between urban heat islands and heat waves: the impact in cities is larger than the sum of its parts. J Appl Meteorol Climatol 52:2051–2064. https://doi.org/10.1175/JAMC-D-13-02.1

Li Q, Bou-Zeid E (2019) Contrasts between momentum and scalar transport over very rough surfaces. J Fluid Mech 880:32–58. https://doi.org/10.1017/jfm.2019.687

Li Q, Bou-Zeid E, Anderson W (2016) The impact and treatment of the Gibbs phenomenon in immersed boundary method simulations of momentum and scalar transport. J Comput Phys 310:237–251. https://doi.org/10.1016/j.jcp.2016.01.013

Li Q, Bou-Zeid E, Anderson W, Grimmond S, Hultmark M (2016) Quality and reliability of les of convective scalar transfer at high Reynolds numbers. Int J Heat Mass Transf 102:959–970. https://doi.org/10.1016/j.ijheatmasstransfer.2016.06.093

Li Q, Bou-Zeid E, Grimmond S, Zilitinkevich S, Katul G (2020) Revisiting the relation between momentum and scalar roughness lengths of urban surfaces. Q J R Meteorol Soc 146(732):3144–3164. https://doi.org/10.1002/qj.3839

Li XX, Liu CH, Leung DY, Lam KM (2006) Recent progress in CFD modelling of wind field and pollutant transport in street canyons. Atmos Environ 40(29):5640–5658. https://doi.org/10.1016/j.atmosenv.2006.04.055

Li Z, Zhang H, Wen CY, Yang AS, Juan YH (2020) Effects of frontal area density on outdoor thermal comfort and air quality. Build Environ 180(107):028. https://doi.org/10.1016/j.buildenv.2020.107028

Lim H, Hertwig D, Grylls T, Gough H, Van Reeuwijk M, Grimmond C, Vanderwel C (2022) Pollutant dispersion by tall buildings: laboratory experiments and large-eddy simulation. Exp Fluids. https://doi.org/10.1007/s00348-022-03439-0

Lindberg F, Grimmond C, Gabey A, Huang B, Kent CW, Sun T, Theeuwes NE, Järvi L, Ward HC, Capel-Timms I, Chang Y, Jonsson P, Krave N, Liu D, Meyer D, Olofson KFG, Tan J, Wästberg D, Xue L, Zhang Z (2018) Urban multi-scale environmental predictor (UMEP): an integrated tool for city-based climate services. Environm Model Software 99:70–87. https://doi.org/10.1016/j.envsoft.2017.09.020

Lindberg F, Grimmond C, Gabey A, Järvi L, Kent CW, Krave N, Sun T, Wallenberg N, Ward HC (2019) Urban multi-scale environmental predictor (UMEP) manual

Llaguno-Munitxa M, Bou-Zeid E (2018) Shaping buildings to promote street ventilation: a large-eddy simulation study. Urban Clim 26:76–94. https://doi.org/10.1016/j.uclim.2018.08.006

Llaguno-Munitxa M, Bou-Zeid E, Hultmark M (2017) The influence of building geometry on street canyon air flow: validation of large eddy simulations against wind tunnel experiments. J Wind Eng Ind Aerodyn 165:115–130. https://doi.org/10.1016/j.jweia.2017.03.007

Lu J, Nazarian N, Hart MA, Krayenhoff ES, Martilli A (2023a) Novel geometric parameters for assessing flow over realistic versus idealized urban arrays. J Adv Model Earth Syst 15(7):e2022MS003287. https://doi.org/10.1029/2022MS003287

Lu J, Nazarian N, Hart MA, Krayenhoff ES, Martilli A (2023) Representing the effects of building height variability on urban canopy flow. Q J R Meteorol Soc 150(758):46–67. https://doi.org/10.1002/qj.4584

Lu J, Nazarian N, Hart MA, Krayenhoff ES, Martilli A (2024) A one-dimensional urban flow model with an eddy-diffusivity mass-flux (edmf) scheme and refined turbulent transport (mlucm v3.0). Geosci Model Develop 17(7):2525–2545. https://doi.org/10.5194/gmd-17-2525-2024

Macdonald R (2000) Modelling the mean velocity profile in the urban canopy layer. Boundary-Layer Meteorol 97:25–45. https://doi.org/10.1023/A:1002785830512

Mairaj A, Baba AI, Javaid AY (2019) Application specific drone simulators: recent advances and challenges. Simul Model Pract Theory 94:100–117. https://doi.org/10.1016/j.simpat.2019.01.004

Martilli A, Santiago J, Salamanca F (2013) On the representation of urban heterogeneities in mesoscale models. Environ Fluid Mech. https://doi.org/10.1007/s10652-013-9321-4

Millward-Hopkins J, Tomlin A, Ma L, Ingham D, Pourkashanian M (2012) Aerodynamic parameters of a UK city derived from morphological data. Boundary-Layer Meteorol. https://doi.org/10.1007/s10546-012-9761-2

Mittal R, Iaccarino G (2005) Immersed boundary methods. Annu Rev Fluid Mech 37:239–261

Monahan H, Armendariz M (1971) Gust factor variations with height and atmospheric stability. J Geophys Res 76(24):5807–5818

Nazarian N, Krayenhoff E, Martilli A (2020) A one-dimensional model of turbulent flow through "urban" canopies (mlucm v2.0): updates based on large-eddy simulation. Geosci Model Develop 13:937–953. https://doi.org/10.5194/gmd-13-937-2020

Nesta (2018) Flying high: shaping the future of drones in UK cities

Nfaoui H, Essiarab H, Sayigh A (2004) A stochastic Markov chain model for simulating wind speed time series at tangiers, morocco. Renew Energy 29(8):1407–1418. https://doi.org/10.1016/S0960-1481(03)00143-5

Ng E, Yuan C, Chen L, Ren C, Fung JC (2011) Improving the wind environment in high-density cities by understanding urban morphology and surface roughness: A study in hong kong. Landsc Urban Plan 101(1):59–74. https://doi.org/10.1016/j.landurbplan.2011.01.004

Oke TR, Mills G, Christen A, Voogt JA (2017) Urban climates. Cambridge University Press, Cambridge

OpenStreetMap contributors (2017) Planet dump retrieved from https://planet.osm.org. https://www.openstreetmap.org

Panagiotou I, Neophytou MKA, Hamlyn D, Britter RE (2013) City breathability as quantified by the exchange velocity and its spatial variation in real inhomogeneous urban geometries: An example from central london urban area. Sci Total Environ 442:466–477. https://doi.org/10.1016/j.scitotenv.2012.09.001

Panofsky HA, Dutton JA (1984) Atmospheric turbulence. Models and methods for engineering applications, Wiley, New York

Pardyjak ER, Stoll R (2017) Improving measurement technology for the design of sustainable cities. Measure Sci Technol 28(9):092001

Roth M (2000) Review of atmospheric turbulence over cities. Q J R Meteorol Soc 126(564):941–990. https://doi.org/10.1002/qj.49712656409

Ryu YH, Smith JA, Bou-Zeid E, Baeck ML (2016) The influence of land surface heterogeneities on heavy convective rainfall in the Baltimore-Washington metropolitan area. Mon Weather Rev 144:553–573. https://doi.org/10.1175/MWR-D-15-0192.1

Salizzoni P, Marro M, Soulhac L, Grosjean N, Perkins RJ (2011) Turbulent transfer between street canyons and the overlying atmospheric boundary layer. Boundary-Layer Meteorol 141(3):393–414. https://doi.org/10.1007/s10546-011-9641-1

Schmid MF, Lawrence GA, Parlange MB, Giometto MG (2019) Volume averaging for urban canopies. Boundary-Layer Meteorol 173(3):349–372. https://doi.org/10.1007/s10546-019-00470-3

Shaikh Salim SAZ, Hagishima A, Tanimoto J, Ikegaya N (2011) Aerodynamic parameters of urban building arrays with random geometries. Boundary-Layer Meteorol 138:99–120. https://doi.org/10.1007/s10546-010-9551-7

Simón-Moral A, Santiago JL, Krayenhoff ES, Martilli A (2014) Streamwise versus spanwise spacing of obstacle arrays: parametrization of the effects on drag and turbulence. Boundary-Layer Meteorol 151:579–596

Slotnick JP, Khodadoust A, Alonso J, Darmofal D, Gropp W, Lurie E, Mavriplis DJ (2014) CFD vision 2030 study: a path to revolutionary computational aerosciences. NASA, Tech Rep NASA/CR-2014-218178

Stoll R, Gibbs JA, Salesky ST, Anderson W, Calaf M (2020) Large-eddy simulation of the atmospheric boundary layer. Boundary-Layer Meteorol 177:541–581

Sützl B, Rooney G, Van Reeuwijk M (2021) Drag distribution in idealized heterogeneous urban environments. Boundary-Layer Meteorol. https://doi.org/10.1007/s10546-020-00567-0

Takemi T, Yoshida T, Horiguchi M, Vanderbauwhede W (2020) Large-eddy-simulation analysis of airflows and strong wind hazards in urban areas. Urban Clim 32(100):625. https://doi.org/10.1016/j.uclim.2020.100625

Temmerman L, Leschziner M, Mellen C, Fröhlich J (2003) Investigation of subgrid-scale models and wall-functions approximations in large eddy simulation of separated flow in a streamwise periodic channel constriction. Int J Heat Fluid Flow 24:157–180. https://doi.org/10.1016/S0142-727X(02)00222-9

Tseng YH, Meneveau C, Parlange MB (2006) Modeling flow around bluff bodies and predicting urban dispersion using large eddy simulation. Environ Sci Technol 40(8):2653–2662. https://doi.org/10.1021/es051708m

UN-DESA (2018) World urbanization prospects: The 2018 revision. https://population.un.org/wup/assets/WUP2018-Report.pdf

Verkaik J (2000) Evaluation of two gustiness models for exposure correction calculations. J Appl Meteorol Climatol 39(9):1613–1626

Wang W, Okaze T (2023) Statistical analysis for predicting low-occurrence strong wind speeds at the pedestrian level in an actual urban case. Build Environ 244(110):781. https://doi.org/10.1016/j.buildenv.2023.110781

Wang W, Seta K, Ikegaya N (2022) Modelling probability density functions based on the gram-charlier series with higher-order statistics: Theoretical derivation and application. J Wind Eng Ind Aerodyn 231(105):227. https://doi.org/10.1016/j.jweia.2022.105227

Wieringa J (1973) Gust factors over open water and built-up country. Boundary-Layer Meteorol 3(4):424–441

Xie ZT, Castro IP (2009) Large-eddy simulation for flow and dispersion in urban streets. Atmos Environ 43(13):2174–2185

Yuan C, Ng E (2012) Building porosity for better urban ventilation in high-density cities - a computational parametric study. Build Environ 50:176–189. https://doi.org/10.1016/j.buildenv.2011.10.023

Zahn E, Bou-Zeid E (2024) Setting up a large-eddy simulation to focus on the atmospheric surface layer. Boundary-Layer Meteorol. https://doi.org/10.1007/s10546-023-00841-x

Zhou Q (2017) Digital elevation model and digital surface model. International Encyclopedia of Geography: People, the Earth, Environment and Technology, pp 1–17. https://doi.org/10.1002/9781118786352.wbieg0768

Zhu X, Anderson W (2018) Turbulent flow over urban-like fractals: prognostic roughness model for unresolved generations. J Turbul 19(11–12):995–1016. https://doi.org/10.1080/14685248.2019.1568446

Zhu X, Iungo GV, Leonardi S, Anderson W (2017) Parametric study of urban-like topographic statistical moments relevant to a priori modelling of bulk aerodynamic parameters. Boundary-Layer Meteorol 162(2):231–253. https://doi.org/10.1007/s10546-016-0198-x